Acta Pharmaceutica Sinica B 2022;12(3):1363−1376

Chinese Pharmaceutical Association
Institute of Materia Medica, Chinese Academy of Medical Sciences

Acta Pharmaceutica Sinica B

www.elsevier.com/locate/apsb
www.sciencedirect.com

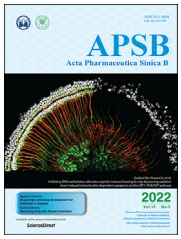

ORIGINAL ARTICLE

Whole-body PET tracking of a D-dodecapeptide and its radiotheranostic potential for PD-L1 overexpressing tumors

Kuan Hu[a,1], Wenyu Wu[b,1], Lin Xie[a], Hao Geng[c], Yiding Zhang[a], Masayuki Hanyu[a], Lulu Zhang[a], Yinghuan Liu[c], Kotaro Nagatsu[a], Hisashi Suzuki[a], Jialin Guo[f], Yundong Wu[c,e,*], Zigang Li[c,d,*], Feng Wang[b,*], Mingrong Zhang[a,*]

[a]*Department of Advanced Nuclear Medicine Sciences, National Institute of Radiological Sciences, National Institutes for Quantum and Radiological Science and Technology, Chiba 263-8555, Japan*
[b]*Department of Nuclear Medicine, Nanjing First Hospital, Nanjing Medical University, Nanjing 210006, China*
[c]*State Key Laboratory of Chemical Oncogenomics, the School of Chemical Biology and Biotechnology, Peking University, Shenzhen Graduate School, Shenzhen 518055, China*
[d]*Pingshan Translational Medicine Center, Shenzhen Bay Laboratory, Shenzhen 518118, China*
[e]*Institute of Chemical Biology, Shenzhen Bay Laboratory, Shenzhen 518038, China*
[f]*Rensselaer Polytechnic Institute, Troy, NY 12180, USA*

Received 13 July 2021; received in revised form 2 September 2021; accepted 14 September 2021

KEY WORDS

D-peptide;
PET imaging;
Radiotheranostics;
In vivo fate;
PD-L1

Abstract Peptides that are composed of dextrorotary (D)-amino acids have gained increasing attention as a potential therapeutic class. However, our understanding of the *in vivo* fate of D-peptides is limited. This highlights the need for whole-body, quantitative tracking of D-peptides to better understand how they interact with the living body. Here, we used mouse models to track the movement of a programmed death-ligand 1 (PD-L1)-targeting D-dodecapeptide antagonist (DPA) using positron emission tomography (PET). More specifically, we profiled the metabolic routes of [^{64}Cu]DPA and investigated the tumor engagement of [^{64}Cu/^{68}Ga]DPA in mouse models. Our results revealed that intact [^{64}Cu/^{68}Ga]DPA was primarily eliminated by the kidneys and had a notable accumulation in tumors. Moreover, a single dose of [^{64}Cu]DPA effectively delayed tumor growth and improved the survival of mice. Collectively,

*Corresponding authors. Tel./fax: +81 43 3823709 (Mingrong Zhang), +86 25 52271455 (Feng Wang), +86 755 26033616 (Zigang Li), +86 755 26611113 (Yundong Wu).
E-mail addresses: wuyd@pkusz.edu.cn (Yundong Wu), lizg@pkusz.edu.cn (Zigang Li), fengwangcn@hotmail.com (Feng Wang), zhang.ming-rong@qst.go.jp (Mingrong Zhang).
[1]These authors made equal contributions to this work.
Peer review under responsibility of Institute of Materia Medica, Chinese Academy of Medical Sciences and Chinese Pharmaceutical Association.

https://doi.org/10.1016/j.apsb.2021.09.016

these results not only deepen our knowledge of the *in vivo* fate of D-peptides, but also underscore the utility of D-peptides as radiopharmaceuticals.

1. Introduction

Peptides possess many favorable properties that make them exceptionally attractive as therapeutic agents for the treatment of a host of diseases. These include their high binding affinities, low toxicities and immunogenicities, and remarkable target specificities. Their sequence and structure diversity also affords very broad coverage across a range of drug targets[1−3]. Although peptides possess these key advantages, unmodified peptides are susceptible to protease degradation and rapid renal excertion[4]. Consequently, they usually have prohibitively poor *in vivo* half-lives, which severely limits their clinical use. Given this, the dextrorotary (D)-peptide strategy has been extensively utilized across a range of applications as an effective mediator for the poor stability of levorotary (L)-peptides[5−7].

D-peptides are hyper-resistant to proteolytic degradation in L-homochiral, living subjects, owing to the variations in geometric profiles caused by changes in backbone-side chain connectivity[8−10]. As a result, D-peptides have remarkably prolonged gut, blood plasma, and intracellular half-lives[5,11−13]. Moreover, D-peptides mostly retain the original binding abilities of their L-counterparts. Comparatively, other peptide stabilization strategies, such as stapling[14], macrocyclization[15], and foldamer[16], which may lead to unavoidable conformational variations that adversely destroy their native binding patterns. Furthermore, other stabilization strategies often reduce peptide solubilities while D-analogs usually do not change them. Last but not least, several D-residue-presenting peptides have been approved for use in patients, indicating that D-analogs are well tolerated in humans[17]. Given these compelling advantages presented by D-peptides, a variety of methods to generate D-peptide ligands have been established for various disease targets. Two elegant methods that have been used for D-peptide ligand discovery are mirror-image phage display (MIPD, Scheme 1A)[18] and retro-inversion (Scheme 1B)[19]. The feasibility and utility of each of these methods have been demonstrated across many applications, such as PPI modulation[20−24], brain-targeted drug delivery[25], immune checkpoint blockade therapy[26,27], and others[28−32].

Theoretically, D-peptides are ideal drug candidates; however, there remain many uncertainties regarding their *in vivo* fates and metabolic profiles (Scheme 1C). As D-peptides suffer almost no degradation in the living body, their *in vivo* behavior (*e.g.*, pharmacokinetics, pharmacodynamics, and bioavailability) has been speculated to be significantly different from that of L-peptides[33−36]. However, there currently exists no research regarding the *in vivo* profile of D-peptides. Although several pioneering, proof-of-concept animal studies have demonstrated the utility of D-peptides, the semiquantitative imaging approaches used provide only limited information about the *in vivo* behavior of D-peptides. Given this, positron emission tomography (PET) is considered as a non-invasive imaging technique that sensitively, quantitatively, and dynamically tracks various drug molecules-even at the level of the single cell-throughout the entire body[37]. Moreover, various peptide radiolabeling methods have also been well documented[38−40]. Therefore, PET imaging provides an ideal tool to study the *in vivo* behavior of D-peptides; ultimately, this approach may help deepen our understanding of the inherent properties of D-peptides.

Here, we reported the PET tracking of a programmed death-ligand 1 (PD-L1)-targeting D-dodecapeptide antagonist (DPA) and its binding to PD-L1 inside normal and tumor-bearing mice (Scheme 1D). We first studied the pharmacokinetics of [^{64}Cu]DPA in normal mice, after which we focused on DPA's ability to bind to PD-L1 in PD-L1-overexpressing tumors. For the latter, we used either ^{64}Cu or ^{68}Ga PET imaging in multiple animal models to verify that ^{68}Ga and DPA were well-paired as a PET tracer to gauge PD-L1 tumor expression. We also showed that a single injection of [^{64}Cu]DPA (2 mCi/per mouse) both delayed tumor growth in a xenograft glioma model and extended overall survival. In addition to its therapeutic efficacy, [^{64}Cu]DPA (3 mCi per mouse) had negligible side effects in normal mice, indicating that [^{64}Cu/^{68}Ga]DPA has good potential for use as a radiotheranostics pair for PD-L1 imaging-guided cancer radiotherapy.

2. Materials and methods

2.1. Materials

All chemicals for peptide synthesis and radiolabeling were obtained from Wako Pure Chemical Industries (Osaka, Japan), Macrocyclics (Dallas, TX, USA), or Merck (Darmstadt, Germany). ^{64}Cu was produced in-house at QST (Chiba, Japan) with up to 98% radionuclidic purity. ^{68}Ga was produced in-house at Nanjing First Hospital (Nanjing, China) by a ^{68}Ge/^{68}Ga generator (ITM, Munich, Germany). The radio highperformance liquid chromatography (HPLC) was conducted with a JASCO HPLC system (Tokyo, Japan), which was equipped with a NaI(Tl) Scintillation Radiation Detectors (Ohyo Koken Kogyo Co., Ltd., Tokyo, Japan). For the HPLC column, a 4.6 mm i.d. × 150 mm YMC-Triat-C18 column (Waters, Milford, MA, USA) was used. The eluent conditions are: flow rate: 1 mL/min; 0.1% trifluoroacetic acid (TFA) containing HPLC-grade water as solvent A and 0.1% TFA containing acetonitrile as solvent B; starting with a ratio of A:B = 90:10 to the end ratio of A:B = 100:0 at 20 min. In cell-based and animal-based experiments a 480 Wizard autogamma counter was employed to detect the radioactivity (counts per minute, CPM). To measure the radioactivity injected into the mouse, we used a IGC-7 Curiemeter (Aloka, Tokyo, Japan) for measurement. BMS202 was purchased from Selleck (CAS No. 1675203-84-5, TX, USA). Fluorescein isothiocyanate (FITC) anti-human CD274 (B7-H1, PD-L1) antibody (cat. 393606) and FITC anti-human IgG Fc antibody (cat. 409310) were purchased from Biolegend (San Diego, CA, USA). Anti-PD-L1 was purchased from Wuhan Proteintech (cat. 17952-1-ap, rabbit anti-human, 1:500 for use). HRP labeled goat anti-rabbit

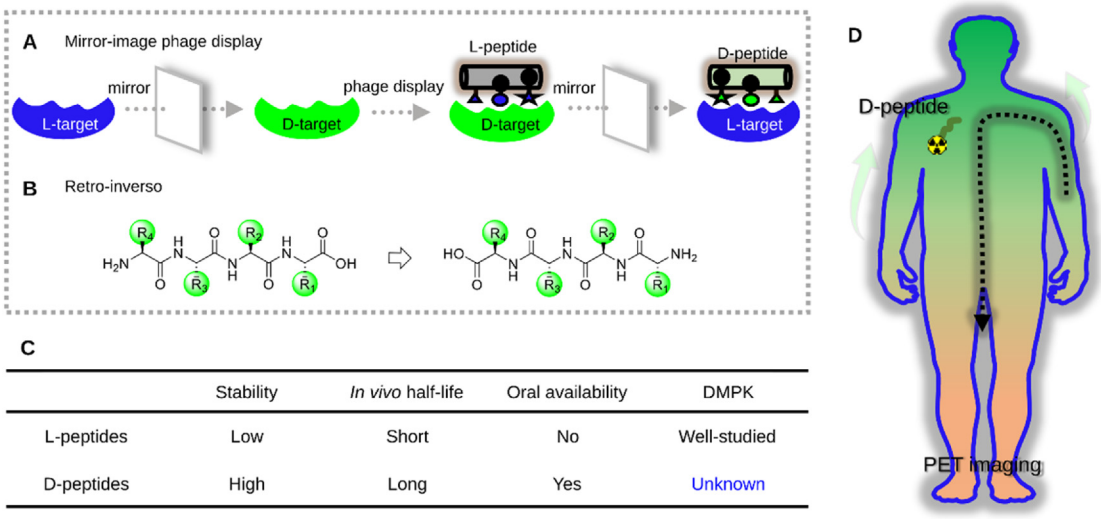

C

	Stability	*In vivo* half-life	Oral availability	DMPK
L-peptides	Low	Short	No	Well-studied
D-peptides	High	Long	Yes	Unknown

Scheme 1 Methods for generating D-type lead peptides and whole-body tracking of D-peptides *via* PET imaging. (A) Mirror-image phage display for generating highly potent D-peptides for target binding. (B) Structure of a tetrapeptide and its retro-inverse analog. (C) Comparison of L-peptides with D-peptides in terms of pharmacological properties. DMPK: drug metabolism and pharmacokinetics. (D) Whole-body tracking of D-peptides for *in vivo* fate study using PET imaging.

second antibody was purchased from Servicebio (cat. GB23303, 1:200 for use). Rabbit anti-Ki-67 monoclonal antibody was purchased from Abcam (cat. ab16667, 1:500 dilution; cross-reactivity for mouse and human; Cambridge, UK). Anti-PCNA antibody was purchased from Abcam (cat. ab29, 1:500 dilution; cross-reactivity for mouse and human; Cambridge, UK).

2.2. *Cell lines and animals*

Three cell lines (mouse melanoma B16F10, human glioblastoma U87MG, and human pancreatic serotonin-producing neuroendocrine tumor Bon-1) were purchased from the ATCC (VA, USA) and cultured at 37 °C in a humidified incubator supplemented with 5% CO_2. Complete Dulbecco's Modified Eagle Medium (DMEM) medium (supplied with 10% fetal bovine serum (FBS) + 1% of penicillin/streptomycin) was used to culture cells.

For animal experiments, we treated animals with human care and conducted experiments strictly following the instructions of the Committee for the Care and Use of Laboratory Animals, NIRS. The Animal Ethics Committee of the QST approved all the experimental plans and procedures. 7-week-old mice (BALB/c nude$^{-/-}$ or C57BL/6J Jms) were obtained from Japan SLC Ltd. (Shizuoka, Japan). C57BL/6J mice inoculating B16F10 allograft were prepared by subcutaneously injecting 1×10^6 cells into the left flank of each mouse. Similarly, BALB/c nude$^{-/-}$ mice inoculating U87MG or Bon-1 xenograft were prepared by subcutaneously injecting 5×10^6 cells into the left flank or hind legs of each mouse.

2.3. *Synthesis of DPA-DOTA peptide*

A Fmoc-based solid-phase peptide synthesis strategy was used to synthesize the DPA-DOTA peptide, as illustrated in Supporting Information Scheme S1. The synthetic procedures were performed as previously described[41,42]. 1,4,7,10-Tetraazacyclododecane-1,4,7,10-tetraacetic acid (DOTA) was used for ^{68}Ga and ^{64}Cu chelation and was conjugated to the N-terminal of the peptide. After synthesis, the DPA-DOTA was purified and lyophilized, and stored at −20 °C. The FITC-labeled DPA was synthesized by replacing the DOTA with a FITC. Specifically, 4 equiv. of fluorescein isothiocyanate and 8 equiv. of DIEA were dissolved in dimethylformamide (DMF); subsequently, the cocktail was added to the swelled resin. After 2 h reacting under N_2 protection, the resin was washed and shrank using methanol. Finally, the FITC-DPA (Supporting Information Scheme S2) was obtained with >98% purity.

2.4. *Radionuclide labeling*

The radiolabeling of DPA-DOTA with ^{64}Cu and ^{68}Ga has used the methods as previously described[41]. Briefly, for ^{64}Cu labeling, an aliquot of 10 μg DPA-DOTA peptide dissolved in 5 μL NaOAc buffer (0.1 mol/L, pH 5.0) was added to 185 MBq (5 mCi) $^{64}CuCl_2$ in 100 μL NaOAc (0.1 mol/L, pH 5). The solution was agitated for 10 s and then incubated in a preheated incubator at 80 °C for 5−10 min. Finally, the mixture was cooled down to room temperature and subjected to quality control by radio-HPLC. Similarly, for ^{68}Ga labeling, an aliquot of 10 μg DPA-DOTA dissolved in 5 μL sodium acetate buffer (0.1 mol/L, pH 5.0) was added to 200 MBq [^{68}Ga]$GaCl_3$ (in 0.6 mol/L HCl, 400 μL), and adjust the pH to 4−4.5. The solution was incubated at room temperature for 5−10 min. Afterward, the reaction mixture was subjected to quality control by radio-HPLC.

2.5. *Peptide stability assays*

To test the [^{64}Cu]DPA's stability in saline, 10 μL radiotracers (~100 μCi, in NaOAc) was added to 990 μL saline and incubated at 37 °C. Aliquots of the solution were withdrawn at assigned time points and then injected into the radio-HPLC for analysis. To test the [^{64}Cu]DPA's stability in mouse serum, 10 μL radiotracers (~100 μCi) were mixed with 90 μL mouse serum (freshly prepared). The mixture was incubated in a 37 °C water bath for different periods. Aliquots (20 μL) of the mixture were withdrawn at designated time points (1, 2, and 4 h) and added to 100 μL 50%

acetonitrile solution (by volume). The precipitate was removed by ultracentrifugation for 10 min (at 10,000 rpm). The supernatant was subjected to HPLC analysis.

2.6. Partition coefficient test

In a 2 mL Eppendorf tube, 500 μL PBS (0.01 mol/L, pH 7.4) or ultrapure water was added, followed by adding 0.5 MBq (5 μL) [^{64}Cu]DPA and 500 μL 1-octanol, sequentially. The two-phase system was thoroughly mixed by vigorous shake for 2 h at room temperature. Then the tubes were subjected to centrifugation (15,000 rpm) for 1 min to ensure complete solvent separation. Aliquots of (100 × 3) of the water and organic phase were separately withdrawn. The radioactivity of each tube was measured in a gamma counter. The partition coefficient (*c*log*D*) was calculated based on Eq. (1):

$$c\mathrm{Log}D = \mathrm{Lg}(\mathrm{CPM\ in\ 1\text{-}octanol/CPM\ in\ aqueous\ solution}) \quad (1)$$

2.7. Determination of in vivo metabolites

Normal C57BL/6J mice (7 weeks old) were intravenously injected with 18.5 MBq [^{64}Cu]DPA (corresponding to 1−5 μg DPA-DOTA per mouse). Mice were sacrificed, and the urine was withdrawn from the bladder at designated time points (0.5, 2, and 24 h after injection). The proteins in the urines were precipitated by adding an equal volume of acetonitrile and removed by centrifugation. The supernatant was analyzed by radio HPLC. The urine samples were also analyzed by radio thin layer chromatography (TLC). 2−2.5 μL urine samples were loaded on TLC Partisil® RP plates (Whatman Inc., Clifton, NJ, USA); ethylenediaminetetraacetic acid (0.05 mol/L) was used as the running buffer to separate the radioactive components. Finally, the TLC plate was imaged by a bioimaging analyzer (FLA-5000IR; Fujifilm, Tokyo, Japan).

2.8. Fluorescent binding assay

B16F10 cells were grown in live-cell imaging dishes (35 mm) with a glass bottom. When the cells grew to about 80% confluency, FITC-DPA (5 μmol/L) in a free DMEM medium was used to replace the old medium. Following 1 h incubation (at 37 °C, 5% CO_2), the cells were briefly washed twice with PBS (37 °C). Afterward, the cells were immersed in a DMEM medium and subjected to fluorescent imaging with a BZ-X700 microscope (Keyence, Osaka, Japan).

2.9. Cellular uptake and competitive binding assay

The B16F10 cells and U87MG cells were seeded in 12-well plates. When the cells reach 80% confluency, [^{64}Cu]DPA (20 μCi/mL) was added. Then the cells were maintained at 37 °C for different periods (5, 20, 40, 60, and 120 min). After that, a pipette was used to withdraw the medium, and cold PBS was used to wash the cells triplicate. To de-attach the cells, 0.5 mol/L NaOH solution (300 μL per well) was added and the cell lysate was collected in 1 mL tubes. The cell-associated radioactivity was measured by an autogamma counter. For the competitive binding assay, unlabeled DPA-DOTA (1 mmol/L), anti-PD-L1 (1 mmol/L), or BMS202 (0.1 mmol/L) were used as PD-L1 inhibitors. For the binding affinity (K_i) measurement, radiotracers were co-incubated with different concentrations of DPA-DOTA, anti-PD-L1, or BMS202; the specific uptake of the tracers by cells after 2 h incubation was normalized to % of specific binding (cellular uptake without inhibitor was set to 100%). The binding affinity was simulated using Prism 8.0 software.

2.10. Flow cytometry analysis of PD-L1 expression

We performed this experiment based on the method as previously described[43]. Briefly, 1 × 10^6 U87MG cells were suspended in 1 mL PBS, then a FITC-conjugated PD-L1-specific antibody (20 nmol/L) (FITC antihuman PD-L1 Antibody, Biolegend, San Diego, USA) was added and followed by incubation at 4 °C for 1 h. Afterward, cells were centrifuged at 1500 rpm for 5 min, washed twice with cold PBS and analyzed on a BD LSRII flow cytometer (Becton Dickinson, NJ, USA). The results were analyzed using FlowJo software (Becton Dickinson, NJ, USA).

2.11. Immunocytochemistry

U87MG cells grew to 80% confluency in a 12-well plate, and were washed with cold PBS triplicate. Then 1% BSA buffer (in PBS) was used to treat cells for 45 min at room temperature. Followed that, the cells were treated with primary anti-PD-L1 monoclonal antibody (mAb) (at 1 μg/mL in 0.1% BSA buffer) for 30 min at room temperature. After that, the cells were washed with 0.1% BSA buffer 4 times, and treated with the secondary antibody. Finally, the cells were washed and subjected to a fluorescent microscopy.

2.12. Ex vivo biodistribution

Formulated tracer (1.85 MBq in 100 μL saline) was intravenously administered into C57BL/6J normal mice or U87MG-bearing BALB/c nude mice. Mice were sacrificed and the whole blood and major organs, were collected at weighted at designated time points (n = 3). Organs associated radioactivity were counted by an autogamma counter, and the decay-corrected % ID/g of each organ was calculated.

2.13. PET study

PET scans were performed as previously described[42,43]. For dynamic scan, the formulated [^{64}Cu]DPA (10−17 MBq in 100−200 μL saline) were intravenously administered *via* a tail vein catheter. Maximum intensity projection (MIP) PET images, co-registered PET-CT images, and the quantification of radioactivity in interested organs were processed using ASIPro VM software (Siemens Medical Solutions, Siemens, Munich, Germany). All data were decay-corrected to the time point of injection.

2.14. Radiotherapy

For xenografting therapy, 5 × 10^6 cells in a mixture of 80 mL free DMEM medium and 20 mL of Matrigel (phenol red-free; Corning, New York, USA) were administered subcutaneously into the left flank of mice. The tumor size was measured using a caliper and calculated as Eq. (2):

$$\mathrm{Volume} = (\mathrm{Length} \times \mathrm{Width}^2)/2 \quad (2)$$

Tumor-bearing mice (n = 5 for control and n = 6 for [^{64}Cu]DPA) were injected with activities of either [^{64}Cu]DPA (2 mCi per mouse) or saline solution on day 6 post-injection. The

experimental endpoint was defined as a tumor volume surpassing 1000 mm^3. Besides this, if other serious clinical symptoms (*e.g.*, 20% weight loss and tumor ulceration) occur, the mouse was also sacrificed. During the therapy period, mouse body weight was determined every three or four days. At the end of therapy (day 23), tumor tissues were collected for further evaluation.

2.15. *In vivo toxicity*

Eight healthy male C57BL/6Jms mice (6 weeks old) were used for toxicity study. The mice were separated into two groups and were injected with different agents (group 1: 100 μL saline; group 2: 3 mCi [^{64}Cu]DPA in 100 μL saline). All the injections were *via* the tail vein. For hematological analysis, 5 μL fresh blood was drawn out from the tail on days 1, 15, and 30 following injection. Then, the blood was diluted into a special buffer for analysis. At the end of the treatment, the liver, spleen, kidney, heart, and lung were collected and fixed in 10% neutral buffered formalin. The fixed organs were next subjected to H&E staining.

2.16. *Histologic analysis*

PD-L1 expression in the tumors was evaluated by immunohistochemistry. The glioma tissues were fixed in 4% paraformaldehyde and paraffin-embedded for sectioning. Then, the samples were dewaxed and hydrated with xylene and alcohol gradients at room temperature before heat-induced antigen retrieval. After, 3% H_2O_2 solution was used to inactivate the activity of endoperoxides and 3% BSA was used to block the non-specific sites. The slides were treated with primary antibody at 4 °C overnight and then with the secondary antibody. Followed that, the sections were stained with 3,3-diaminobenzidine (DAB) and counterstaining with hematoxylin solution for 2 min. Finally, the samples were dehydrated and mounted with neutral resin. All images were acquired using optical microscopy (Nikon Eclipse E100, Tokyo, Japan).

2.17. *Statistical analysis*

Data were analyzed using Prism version 8.0 software (GraphPad Software, La Jolla, CA, USA). Comparisons among groups were performed using two-way ANOVA with Bonferroni's multiple comparisons posttest or unpaired two-tailed Student's *t*-test. Data are presented as the mean ± SEM. or the mean ± SD. The threshold for statistical significance was set as $^{*}P < 0.05$.

3. Results and discussion

3.1. *Radiolabeling of DPA with ^{64}Cu and PET imaging in normal mice*

The peptides' *in vivo* behavior is synergistically modulated by multiple factors, including molecular size, formal charge, and

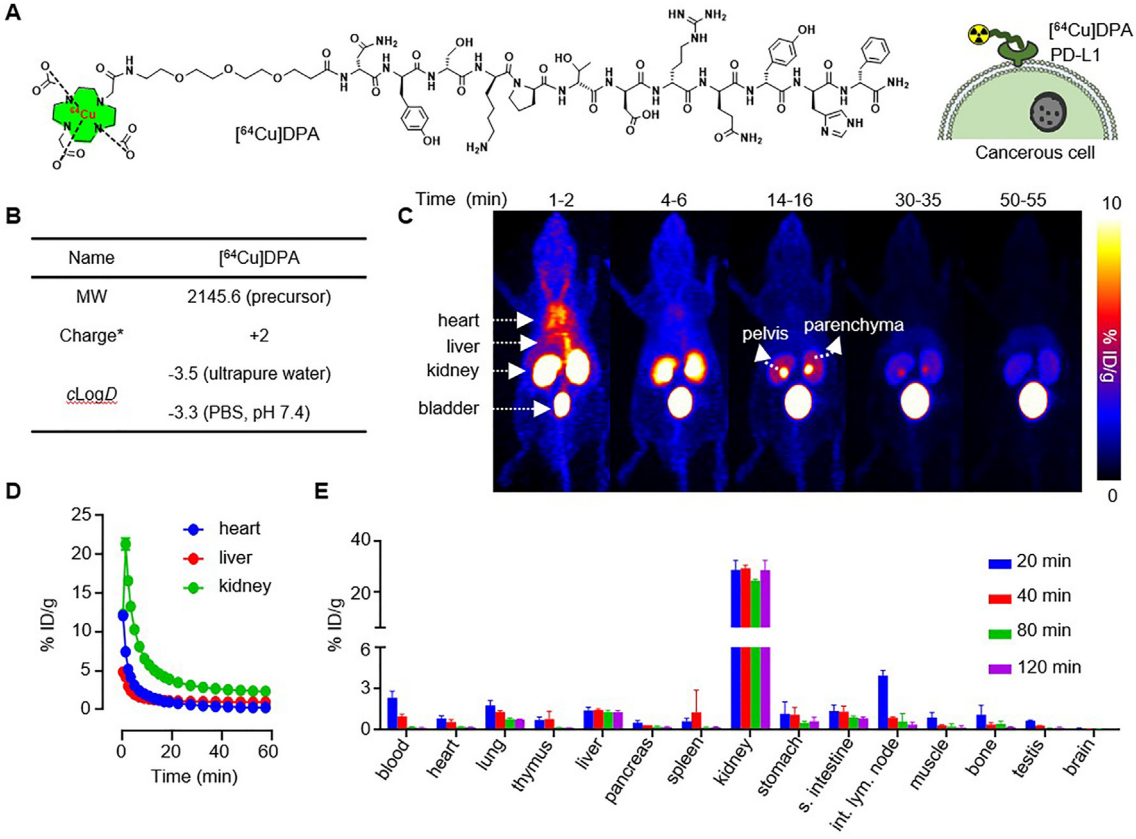

Figure 1 [^{64}Cu]DPA PET in normal mice. (A) Chemical structure of [^{64}Cu]DPA and its binding to PD-L1 overexpressed cancer cells. (B) Physicochemical characteristics of [^{64}Cu]DPA. MW: molecular weight, *at pH 7.4, 25 °C. (C) Series of PET images for C57BL/6J mice at indicated time points after intravenous injection of approximately 0.5 mCi [^{64}Cu]DPA in saline. (D) Time–activity curves (0−60 min) of the heart, liver, and kidney of the mice shown in (C). (E) *Ex vivo* biodistribution data of major organs in C57BL/6J mice at 20, 40, 80, and 120 min post-injection of [^{64}Cu]DPA. $n = 3$, data represent mean ± SD.

lipophilicity[44]. Despite this, we did not explore how these factors impacted the *in vivo* behavior of D-peptides. Instead, we selected a model peptide-DPA for the study[27]. This peptide was identified by MIPD and was shown to be an effective PD-L1 antagonist. DPA was chosen here owing to several considerations. First, DPA is a dodecapeptide, which has the average length of a typical peptide inhibitor. Therefore, choosing DPA would offer the best information regarding the average, *in vivo* behavior of D-peptides[45]. Second, DPA is positively charged and hydrophilic under physiological conditions. These properties afford its good solubility and the ability to avoid nonspecific aggregation in blood. Moreover, DPA's targeting ability and distribution have been semi-quantitatively characterized using fluorescence imaging. The results of these studies served as qualitative references to our PET analysis[27]. Last but not least, PD-L1 is a remarkable target for immune checkpoint blockade therapy, and its overexpression has been implicated in therapeutic outcomes[46]. Given this, the development of D-peptide-based PET tracers for gauging PD-L1 expression has great clinical significance.

To radiolabel DPA with ^{64}Cu ($t_{1/2}$ = 12.7 h), we synthesized DOTA-PEG_3-DPA (Fig. 1A), in which DOTA was a chelator for ^{64}Cu radiolabeling and PEG_3 was a linker to space the DOTA and peptide[41−43]. The ^{64}Cu radiolabeling of DOTA-PEG_3-DPA achieved high radiochemical yield (>99%) and radiochemical purity (>98%) (Supporting Information Table S1). [^{64}Cu]DPA was hyperstable in saline and mouse serum; no ^{64}Cu decomposition or peptide hydrolysis was detected after 24-h incubation at 37 °C (Supporting Information Fig. S1). We next measured the partition coefficient of [^{64}Cu]DPA[47]. The calculated *c*log*D* was −3.5 or −3.3 when the aqueous phase was ultrapure water or PBS (pH 7.4), respectively (Fig. 1B). This indicated that [^{64}Cu]DPA was very hydrophilic and can be easily dissolved in the injection buffer[48].

To monitor the *in vivo* behavior of [^{64}Cu]DPA in a living animal, we performed dynamic PET in normal C57BL/6J mice from 0 to 60 min following intravenous injection (i.v.) of [^{64}Cu]DPA. Sequential PET images were extracted from the dynamic PET to track the movement of [^{64}Cu]DPA in the mouse body (Fig. 1C). At 1−2 min after injection, an intense signal was seen in the heart, suggesting a high tracer concentration in the blood. The highest signals were shown in the kidney and bladder, indicating a rapid distribution of the tracer to the kidney. The signal in the heart disappeared approximately 4−6 min after injection. Simultaneously, the signal intensity in the kidney decreased, which followed an increased signal in the bladder. At 14−16 min post-injection, a remarkably high intensity signal was observed in the pelvis of the kidney relative to that of the parenchyma. Notably and with the exception of the first several minutes following injection, the liver signal was at a consistent, low level during the entire study. This suggested that the liver was not the main organ for [^{64}Cu]DPA metabolism, possibly due to the peptide's superb

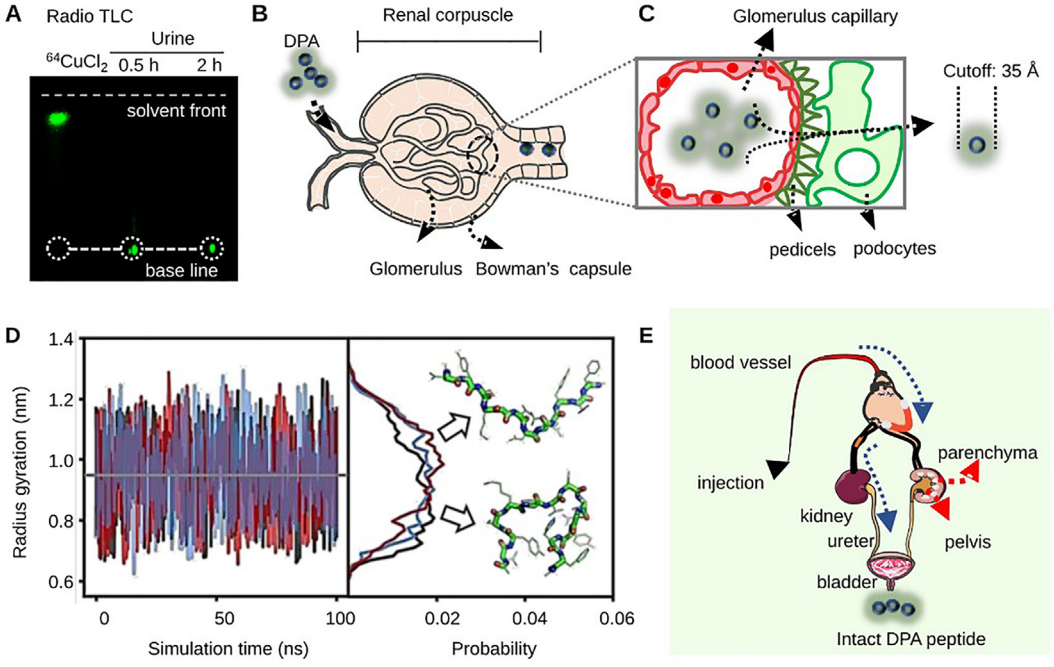

Figure 2 Size-dependent elimination of D-peptides by renal corpuscle. (A) Mouse urine samples were analyzed by radio TLC. Free $^{64}CuCl_2$ was used as a control. (B) An illustration of the anatomic structure of a nephron, which is the functional unit of the kidney. The nephron is built up by renal corpuscle and tubules, where plasma is filtered; filtered fluid then passes through. The renal corpuscle consists of the glomerulus and Bowman's capsule. The former is majorly formed by a capillary network, while the latter is composed of a double-walled epithelial cup that surrounds the glomerulus capillaries. D-peptides entering the renal corpuscle will be filtered by capillaries; filtering depends on their hydrodynamic size. The filtrates will then flow into the bladder through the ureter. (C) A detailed structure of the interface between the glomerulus and glomerular capsules. Glomerular capillaries are encircled with pedicels, which form filtration slits and slit membranes with a cutoff of 42 Å for proteins/peptides. (D) The radius of gyration as a function of simulation time from three independent simulations (black, blue and red). The representative structures and their relative distributions from these simulations (right panel). (E) Proposed tracer flow path of distribution and excretion after intravenous injection.

hydrophilicity. We then performed quantitative PET analysis in the heart, liver, and kidney (Fig. 1D), which indicated that most of the [^{64}Cu]DPA distributed to these organs was eliminated within 20 min post-injection (p.i.).

To comprehensively profile the *in vivo* distribution of the tracer, C57BL/6J mice were used to determine *ex vivo* distribution. Organs were collected from mice at 20, 40, 80, and 120 min p.i. All the studied organs—except for the kidney—showed low tracer uptake and quick elimination (Fig. 1E and Supporting Information Table S2). In the liver and despite low levels of persistent radioactivity, the signal intensity showed no apparent decrease from 20 to 120 min. The kidney showed the highest radioactivity among all studied organs, with levels around 10-fold higher than those observed in the liver. A high tracer uptake was also observed at 20 min p.i. in the intestinal lymph node; however, lymph node levels rapidly decreased at 40 min p.i. These studies were conducted to explore the distribution and elimination of [^{64}Cu]DPA in living animal using PET scanning and anatomic analysis. Collectively, these results suggested that [^{64}Cu]DPA was primarily excreted by renal elimination.

3.2. *Simulation-aided metabolic study of DPA*

To study the metabolic pattern of [^{64}Cu]DPA, mouse urine was collected at different time points p.i. Samples were then analyzed using both HPLC and radio TLC. For urine samples collected from 0.5 to 2 h p.i., only intact [^{64}Cu]DPA was detected (Fig. 2A and Supporting Information Fig. S2). One urine sample with a large enough urine volume to ensure reliability was collected 24 h p.i.; however, it was determined to have negligible levels of radioactivity and was unable to be analyzed.

The renal corpuscle is the place where blood filtration occurs and it provides a precision filtration system that depends on the hydrodynamic size of the substrate[49] (Fig. 2B). For proteins and peptides, a cutoff of 35 Å was estimated to allow for proper filtration from the glomerulus to the ureter[49,50] (Fig. 2C). To more quantitatively investigate DPA's size, we computed the radius of gyration (R_g) of DPA using all-atom molecular dynamics (MD) simulations. Well-converged conformational ensembles were obtained at room temperature (300 K) from three independent, replica-exchange molecular dynamics simulations. These simulations were based on the new RSFF2+ force field[51] with the TIP4P-D water model, a combination that has been shown to provide a more realistic description of disordered peptides[52]. As shown in Fig. 2D, the average and maximum values of DPA's R_g in simulation were 0.95 and 1.30 nm (1.90 and 2.6 nm in diameter), respectively. The representative structures of the peptide in extended and compact conformations are also shown. These results suggest that the peptide was conformationally flexible, and [^{64}Cu]DPA could easily pass through the slit pores. To our knowledge, this is the first, unambiguous demonstration that intact

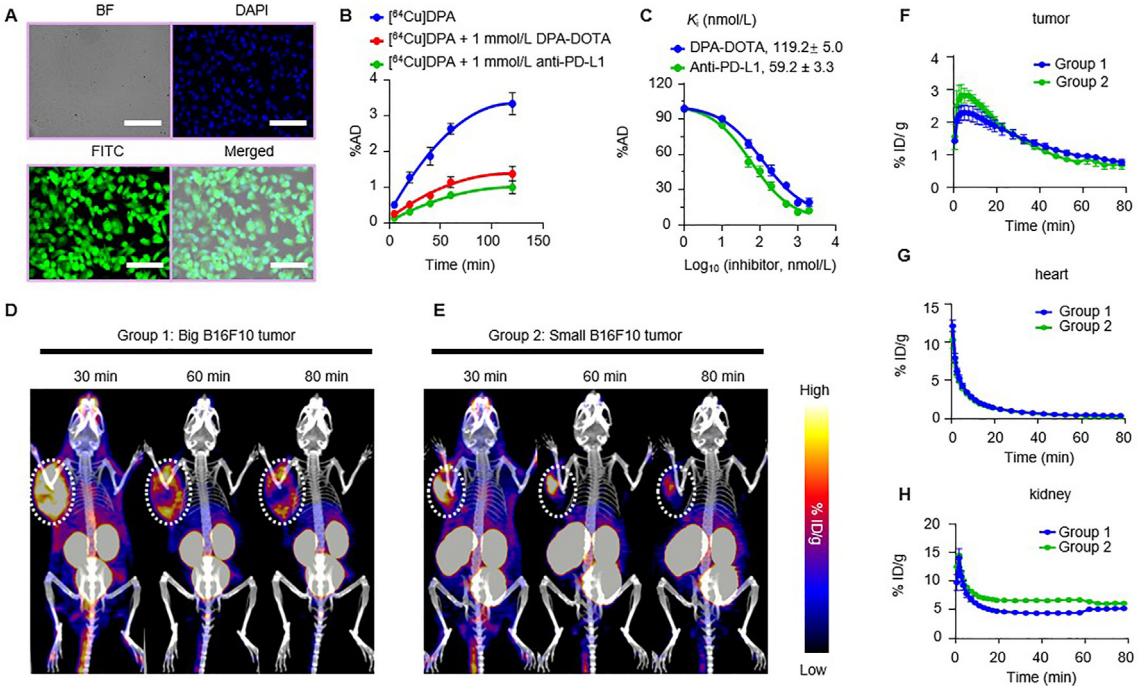

Figure 3 Target engagement study of [^{64}Cu]DPA in tumor models. (A) Fluorescence images of B6F10 cells after co-incubation with 5 μmol/L of FITC-DPA for 1 h at 37 °C. BF: bright field. Scale bar: 100 μm. (B) B16F10 cell uptake of radioactivity when incubation with [^{64}Cu]DPA (20 μCi/mL), [^{64}Cu]DPA (20 μCi/mL) + 1 mmol/L DPA, [^{64}Cu]DPA (20 μCi/mL) + 1 mmol/L anti-PD-L1 for different incubation times. (C) Competitive binding of [^{64}Cu]DPA (20 μCi/mL) to B16F10 cells co-incubated with different concentrations of either DPA or anti-PD-L1 for 120 min at 37 °C. The corresponding K_i values are also shown. (D) and (E) Co-registered PET/CT maximum intensity projection (MIP) images of C57BL/6J mice bearing big B16F10 tumors (D) and small B16F10 tumors (E) after intravenous injection of approximately 0.5 mCi of [^{64}Cu]DPA for 30, 60, and 90 min. The white dashed circles indicate the tumors. (F)–(H) PET image-derived time−activity curves (0−80 min) of B16F10 tumor (F), heart (G), and kidney (H) in C57BL/6J mice bearing B16F10 tumors after intravenous injection of [^{64}Cu]DPA. Groups 1 and 2 correspond to mice shown in panels D and E. Data represent mean ± SD, $n = 3$.

D-peptides were excreted directly through the renal-bladder clearance pathway (Fig. 2E). Moreover, this size-dependent renal clearance implied that changing the hydrodynamic size of D-peptides (multimerization) is a possible way to tune the residence time in a living body.

3.3. PET imaging of PD-L1 with [^{64}Cu]DPA in tumor mouse models

First, we measured the specific binding of DPA to B16F10 melanoma cells (PD-L1 overexpressed). Fluorescence intensity of labeled DPA (FITC-DPA) revealed strong binding to B16F10 cells after 1 h of co-incubation (Fig. 3A). Moreover, the uptake of [^{64}Cu]DPA by B16F10 cells displayed a time-dependent pattern. When non-labeled DPA (1 mmol/L) and a PD-L1 specific antibody (1 mmol/L) were used as blocking agents, significant decreases in the binding portion (%AD) of [^{64}Cu]DPA were observed (Fig. 3B). This result suggested that DPA specifically binds to PD-L1. Finally, the binding affinity (K_i) of [^{64}Cu]DPA to B16F10 cells was determined using a competitive binding assay. The estimated binding affinities were 119 ± 5.0 and 59.2 ± 3.3 nmol/L when DPA and anti-PD-L1 were used as competitors, respectively (Fig. 3C).

Having established its specificity *in vitro*, we next used [^{64}Cu]DPA to image PD-L1 in B16F10 tumor-bearing mice. To test whether [^{64}Cu]DPA was capable of imaging tumors with different volumes, we performed [^{64}Cu]DPA PET in two groups of mice with different tumor volumes (approximately 800 and 200 mm^3, respectively). Mice were imaged following i.v. injection of [^{64}Cu]DPA (Fig. 3D and E). Strong tracer accumulation in tumor sites was observed in both groups of mice at 30, 60, and 80 min p.i. The highest radioactivity in both groups appeared in the kidney and bladder; negligible radioactivity was noted in other tissues, such as the liver and lung. Notably, the tracer showed different distribution patterns in tumors between the two groups. In large tumors, the tracer was primarily distributed at the periphery of the tumor. Comparatively, small tumors saw selective tracer accumulation at the center of the tumor. This phenomenon implies that the [^{64}Cu]DPA is a possible tracer that could be used to map PD-L1 expression heterogeneity. Based on the PET results, we next quantified the radioactivity in the tumor, heart, and kidney (Fig. 3F–H). We obtained almost identical time−activity curves (TACs) between the two groups, indicating that tumor uptake of the tracer was independent of tumor size.

Finally, we performed PET imaging in glioblastoma tumor to generalize [^{64}Cu]DPA PET for use in gauging PD-L1 expression. Past work has shown that high expression of PD-L1 in glioblastoma tumor tissues is correlated to poor patient survival, indicating that PD-L1 may play the role as a prognostic biomarker and a remarkable therapeutic target in glioblastoma[53]. Therefore, the development of non-invasive imaging tools to gauge PD-L1 expression in glioblastoma is an urgent need that would aid in more effective immune checkpoint blockade therapy. We first assayed PD-L1 expression in the U87MG cell line. Flow cytometry results indicated that the subset of PD-L1-expressing cells was approximately 60% across all U87MG cells (Fig. 4A and B). Further PD-L1 fluorescent staining verified this result (Fig. 4C). For *in vivo* PET, when the U87MG tumor volume had reached approximately 100 mm^3, a PET scan was performed following i.v. injection of [^{64}Cu]DPA. At 60 min p.i., strong tracer accumulation in the U87MG tumor was observed (Fig. 4D). PET-derived TAC curves revealed rapid tracer elimination in the blood and kidney. In contrast, the tracer clearance rate in the U87MG tumor was remarkably slower (Fig. 4E), which reflected the tumor specificity of this tracer.

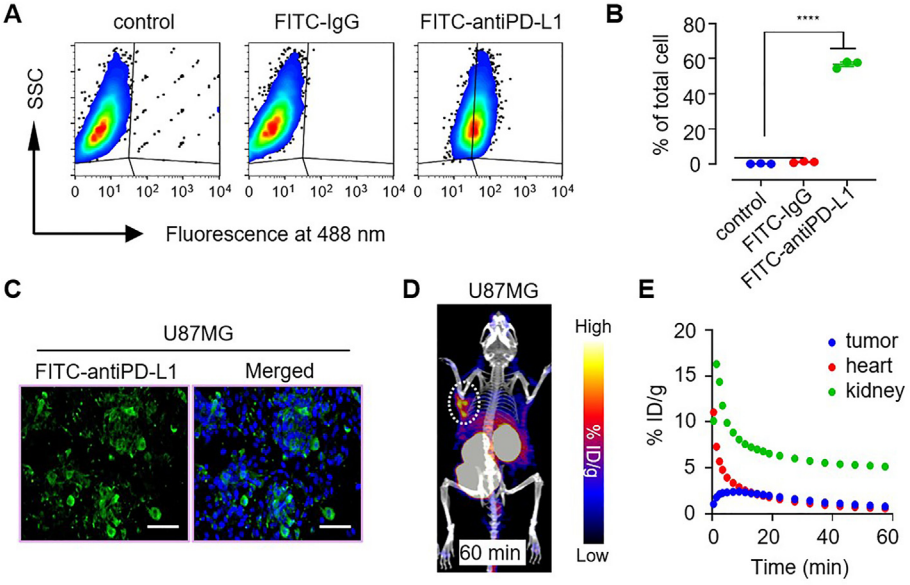

Figure 4 [^{64}Cu]DPA PET imaging of PD-L1 overexpressed U87MG tumor. (A) Flow cytometry analysis of PD-L1 expression in U87MG cell line. SSC: side scatter. (B) PD-L1 positive U87MG cells counted by flow cytometry. Data represent mean ± SD, ****$P < 0.0001$, two-tailed Student's *t*-test. (C) Immunofluorescence imaging of PD-L1 in U87MG cells. Scale bar: 100 μm. (D) Co-registered PET/CT MIP images of BALB/c nude mice bearing U87MG tumors after intravenous injection of approximately 0.5 mCi of [^{64}Cu]DPA for 60 min. The white dashed circle indicates the tumor position. (E) PET image-derived time−activity curves (0−60 min) of U87MG tumor, heart, and kidney in BALB/c nude mice bearing U87MG tumors after intravenous injection of [^{64}Cu]DPA.

3.4. *Radiolabeling of DPA with ^{68}Ga and PET study with [^{68}Ga]DPA*

Gallium-68 is a positron emission radionuclide with a decay half-life of 68 min and has been recognized as an ideal radionuclide to label peptides for PET imaging[54]. ^{68}Ga is produced by using germanium-68/gallium-68 (^{68}Ge/^{68}Ga) generator systems, making it more suitable for use in hospital than ^{64}Cu, which is produced by cyclotron. Moreover, the optimal imaging time for ^{68}Ga is 60−120 min post-injection, which is a time window that perfectly matches the pharmacodynamics profile of DPA in the tumor. These features make ^{68}Ga a better matched radionuclide to pair with DPA for PET imaging when compared with ^{64}Cu. Given this, we labeled DPA with ^{68}Ga with high efficiency (>98%) (Supporting Information Table S1). Similar to [^{64}Cu]DPA, [^{68}Ga]DPA was hyper-stable both in saline and mouse serum after 24-h incubation (Supporting Information Fig. S3). Uptake of [^{68}Ga]DPA into U87MG cells was shown to be time-dependent, and a PD-L1 specific small molecular inhibitor (BMS202) significantly inhibited the uptake of [^{68}Ga]DPA (Fig. 5A). The K_i of [^{68}Ga]DPA in U87MG cells was further assessed using BMS202 as a competitor, which established a binding affinity of 43.8 ± 8.6 nmol/L (Fig. 5B).

We next performed [^{68}Ga]DPA PET imaging in U87MG tumor-bearing BALB/c nude mice. When the subcutaneously inoculated U87MG tumor grew to approximately 100 mm^3, [^{68}Ga]DPA was administrated *via* i.v. injection. Whole-body PET-CT images showed a strong [^{68}Ga]DPA accumulation in the tumor at 30 and 60 min postinjection (Fig. 5C). Similar to [^{64}Cu]DPA, [^{68}Ga]DPA displayed the highest accumulation in the kidney and bladder.

To verify the PD-L1-specific accumulation in the tumor, we next performed a parallel experiment in another cohort of mice inoculated with PanNET cell line Bon-1 (Fig. 5C). We observed little [^{68}Ga]DPA accumulation in Bon-1 tumor at 60 min p.i. To clarify this difference, the tumor tissues were collected and subjected to PD-L1 immunohistochemical analysis. The U87MG tumor section stained with anti-PD-L1 revealed considerable PD-L1 expression (Fig. 5D and F). In contrast, the Bon-1 tumor section showed little PD-L1 expression (Fig. 5E and F), which was consistent with the PET results. To preclude the possibility that this difference in PD-L1 expression was due to different tumor cell growth statuses (*e.g.*, tissue necrosis), we then performed hematoxylin and eosin (H&E) staining of the tumor sections. Similar tumor cell morphology was observed across both sets of tumor tissues (Fig. 5G).

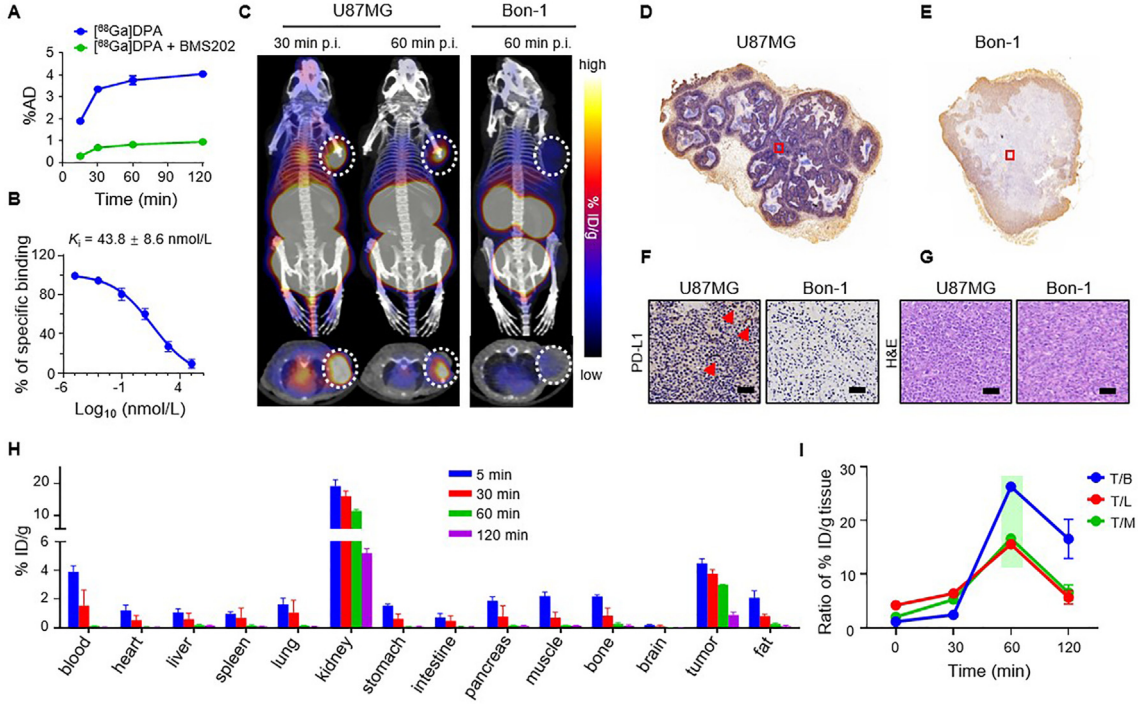

Figure 5 [^{68}Ga]DPA PET imaging of PD-L1 overexpressed U87MG tumor. (A) U87MG cell uptake of radioactivity when incubated with [^{68}Ga]DPA (20 μCi/mL) or [^{68}Ga]DPA (20 μCi/mL) + BMS202 (100 μmol/L) for different periods. (B) Competitive binding of [^{68}Ga]DPA (20 μCi/mL) to U87MG cells co-incubated with different concentrations of BMS202 for 120 min at 37 °C. K_i value is shown in the panel. (C) PET-CT images of U87MG bearing BALB/c nude mice (left panel) and Bon-1 bearing BALB/c nude mice (right panel) treated with approximately 0.5 mCi of [^{68}Ga]DPA. Mice were imaged at 30 min and 60 min after intravenous injection of [^{68}Ga]DPA. Representative MIP (top panel) and transverse PET-CT images (bottom panel) are shown. The white dashed circles indicate the tumor positions. (D) and (E) Whole-section immunohistochemical staining of PD-L1 in U87MG and Bon-1 tumors. (F) Enlarged view of the selected areas in (D) and (E). Scale bar, 100 μm. (G) H&E staining of U87MG and Bon-1 tumor tissues. Scale bar, 100 μm. (H) Biodistribution of [^{68}Ga]DPA in tissue from U87MG bearing BALB/c nude mice measured by gamma counter *ex vivo* after 5, 30, 60, and 120 min intravenous injection of the tracer. $n = 4$ mice per time point. (I) Ratios of tissue uptake of [^{68}Ga]DPA. Values were calculated based on the *ex vivo* biodistribution data in (G). Data are mean ± SD, $n = 4$.

Additionally, we performed an *ex vivo* biodistribution study in U87MG-bearing mice (Fig. 5H and Supporting Information Table S3). Organs from mice intravenously injected with [^{68}Ga]DPA were collected at 5, 30, 60, and 120 min post-injection and were analyzed. [^{68}Ga]DPA exhibited rapid clearance in the blood and most of the analyzed organs, including the heart, liver, lung, and muscle. As the main location for elimination, the kidney showed the highest tracer accumulation and a clearance rate of 0.12% ID/g/min from 5 to 120 min. The tracer uptake in the tumor was revealed to be the second-highest at all tested time points. Moreover, the tumor showed a smaller tracer clearance rate of 0.027% ID/g/min from 5 to 60 min p.i. During the same period, clearance rates were 0.069% and 0.037% ID/g/min for blood and muscle, respectively. Finally, the tumor-to-organ ratio was calculated based on our *ex vivo* biodistribution data. The highest tumor-to-blood (T/B), tumor-to-liver (T/L), and tumor-to-muscle (T/M) ratios co-occurred at 60 min p.i. (Fig. 5I), suggesting that 60−120 min after injection is an optimal time window for PET imaging to achieve the best image quality.

3.5. [^{64}Cu]DPA as a radiopharmaceutical for cancer therapy

Targeted radionuclide therapy (TRT) is an emerging cancer treatment modality that kills cancer cells using a cytocidal, energy-releasing radionuclide, which is brought to the tumor sites through tumor-targeted moieties (*e.g.*, antibody, peptide, or small molecule)[55,56]. As described above, DPA offers key advantages as an ideal radionuclide vector, such as rapid blood clearance and rapid tumor accumulation. Moreover, ^{64}Cu has been shown to be a potential radionuclide for TRT, owing to its emission of β^- and auger electrons[57]. These features make [^{64}Cu]DPA a possible TRT agent for cancer treatment.

We next examined the therapeutic effect of [^{64}Cu]DPA on U87MG tumors. Mice were administrated [^{64}Cu]DPA (approximately 2 mCi per mouse) intravenously on day 6 after tumor inoculation. In the control cohort of mice, an equivalent volume of saline was injected *via* the tail vein (Fig. 6A). Consequently, mice treated with [^{64}Cu]DPA displayed significantly delayed tumor growth compared to the control group (Fig. 6B). Specifically, at day 13 post-injection (equivalent to 19 days post-inoculation), the

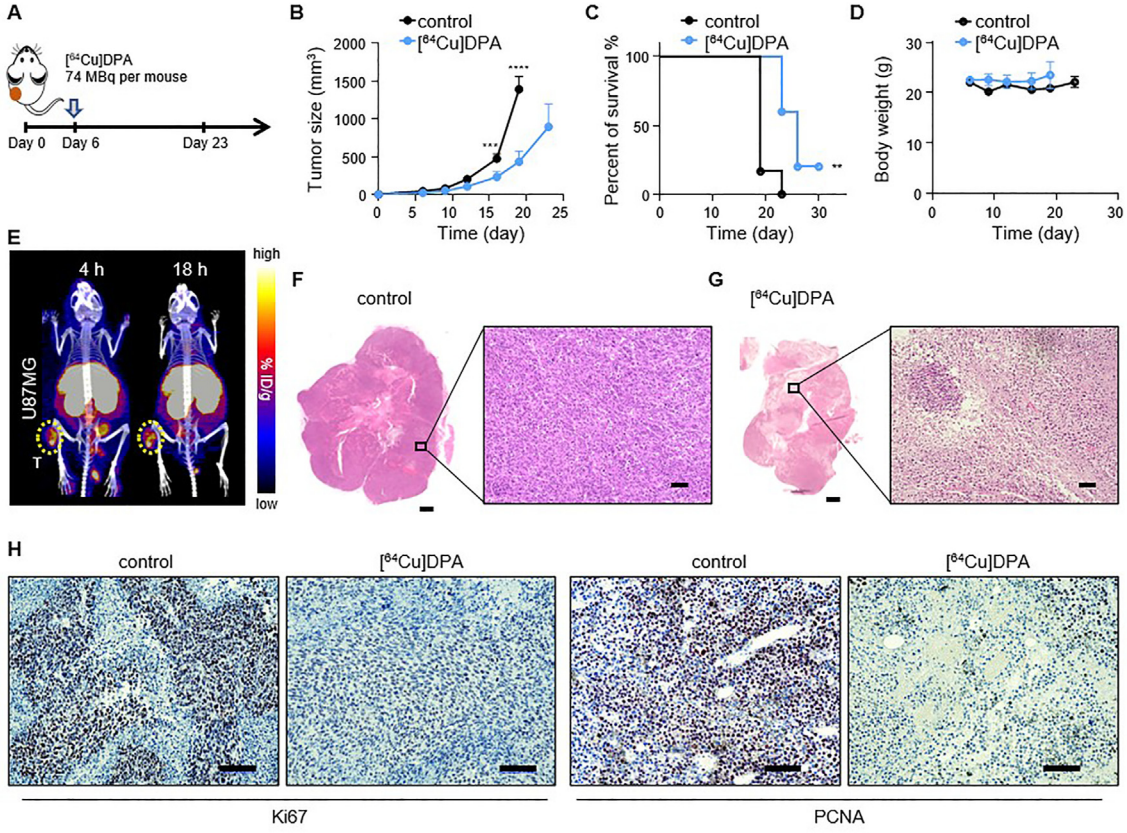

Figure 6 Radionuclide therapy of U87MG tumor with [^{64}Cu]DPA. (A) BALB/c nude mice inoculated with 1×10^6 cells received an intravenous injection of either [^{64}Cu]DPA (~3 mCi in 200 μL saline) or an equivalent of saline on day 6. (B) Tumor growth curves of mice treated with either saline (control) or [^{64}Cu]DPA. $n = 6$ mice for control and $n = 5$ mice for [^{64}Cu]DPA. Data are mean ± SEM. *P* value was calculated using two-way ANOVA. (C) Survival curves of U87MG tumor-bearing BALB/c nude mice treated with saline or [^{64}Cu]DPA. $n = 6$ mice for control and $n = 5$ mice for [^{64}Cu]DPA. Significance was assessed using the log-rank test. (D) Changes in body weight of U87MG tumor-bearing BALB/c nude mice treated with saline or [^{64}Cu]DPA. $n = 4$ mice. (E) PET-CT images of BALB/c nude mice bearing U87MG tumor. Mice were imaged at 4 and 18 h after intravenous injection of [^{64}Cu]DPA. MIP PET-CT images are shown. Yellow dashed circles indicate the tumor positions (left hind legs). (F) and (G) Whole-section H&E staining of U87MG from BALB/c nude mice (left panel). The tumor tissues were harvested on day 23 from mice treated with saline or [^{64}Cu]DPA. Scale bar, 1000 μm. An enlarged view of selected areas was shown at the right panels. Scale bar, 100 μm. (H) Immunohistochemical staining of Ki67 and PCNA in U87MG tumors. The tumor tissues were harvested on day 23 from mice treated with saline or [^{64}Cu]DPA. Scale bar: 200 μm.

average tumor volume of mice in the treated cohort (431.9 mm^3) was significantly smaller than that in the control cohort (1393.1 mm^3; $P < 0.0001$). Simultaneously, the survival of mice treated with [^{64}Cu]DPA was largely improved (Fig. 6C). Mouse body weight was also monitored to check for any acute, detrimental effects of [^{64}Cu]DPA. The body weights of treated mice remained stable during the treatment period and showed no significant variations when compared with the control cohort (Fig. 6D), indicating no noticeably toxic effects.

TRT kills cancerous cells by the delivery of radioactive atoms to tumor-associated targets. However, its efficacy is dependent on multiple factors, including tumor retention time. Although we have demonstrated that [^{64}Cu]DPA rapidly accumulated in the tumor after administration, its retention time in the tumor remained unknown. Given this, we imaged mice at 4 and 18 h after i.v. injection of [^{64}Cu]DPA (Fig. 6E). We observed considerable tracer accumulation in the tumor at both time points.

Finally, to histopathologically verify the therapeutic effect of this approach, we harvested the tumor tissue at the end of therapy and stained it with H&E (Fig. 6F and G). Tumor sections from the [^{64}Cu]DPA treated mice revealed pronounced cell necrosis (Fig. 6G); notably, this phenomenon was rarely observed in tumor samples obtained from control mice (Fig. 6F). In addition, the proliferative ability of tumor cells was analyzed using Ki67 and proliferating cell nuclear antigen (PCNA) staining (Fig. 6H). Tumor tissue from control mice revealed significantly higher Ki67 and PCNA positive rates (67% and 79%, respectively) compared with those from the [^{64}Cu]DPA treated mice (5% and 8%, respectively). Taken together, these results demonstrated [^{64}Cu]DPA is a promising TRT agent for cancer therapy.

3.6. *Toxicity evaluation of [^{64}Cu]DPA*

To assess the potential toxicity of [^{64}Cu]DPA, we assessed an additional two cohorts in normal C57BL/6J mice. In the previous tumor therapy study, we demonstrated a single dose of 2 mCi per mouse exhibited negligible toxicity, as evidenced by consistent body weight changes between the treated and control groups. To test whether an even higher dose would be tolerable, we injected mice with a single dose of 3 mCi per mice (treated group). In the control cohort, each mouse was injected with an equivalent volume of saline. The body weight of each mouse was then measured on day −1 (the day before injection) and on days 1, 3, 7, 15, and 30 after injection. All mice in the treated cohort had no body weight loss during the course of the study, and showed a body weight change that was highly consistent with that of the control cohort (Fig. 7A).

In addition to monitoring body weight changes, we performed a hematological analysis of the mice in both cohorts on days 1, 15, and 30 post-injection. In treated mice, white blood cell (WBC) counts were initially decreased (day 1), but this decrease was minor and not statistically significant (Fig. 7B). Subsequently, WBC levels recovered to those of normal mice on day 15. Interestingly, we observed significantly higher WBC counts in treated mice compared to control mice on day 30. This phenomenon was a possible symptom of radiation pneumonitis, indicating an inflammatory response to radiation[58]. Besides WBC changes, the changes of red blood cells (RBC), hematocrit (HCT), and platelet (PLC) were also examined; there were no significant differences ($P > 0.5$) between the two cohorts (Fig. 7C–E).

To explore whether there were any pathological lesions on the organs caused by the radiation, we performed H&E staining of the heart, kidney, lung, liver, and spleen of representative mice from both cohorts (Fig. 7F). There was no sign of tissue injury in the heart, lung, liver, and spleen, consistent with the rapid clearance of [^{64}Cu]DPA in these organs. As the kidney is the major place for [^{64}Cu]DPA elimination, it is potentially the organ at the highest risk during therapy. However, H&E staining showed neither visualized pathological lesion nor varied size and morphology of the kidney in the treated mice compared with control mice. This result was not unexpected, as [^{64}Cu]DPA was shown to be rapidly

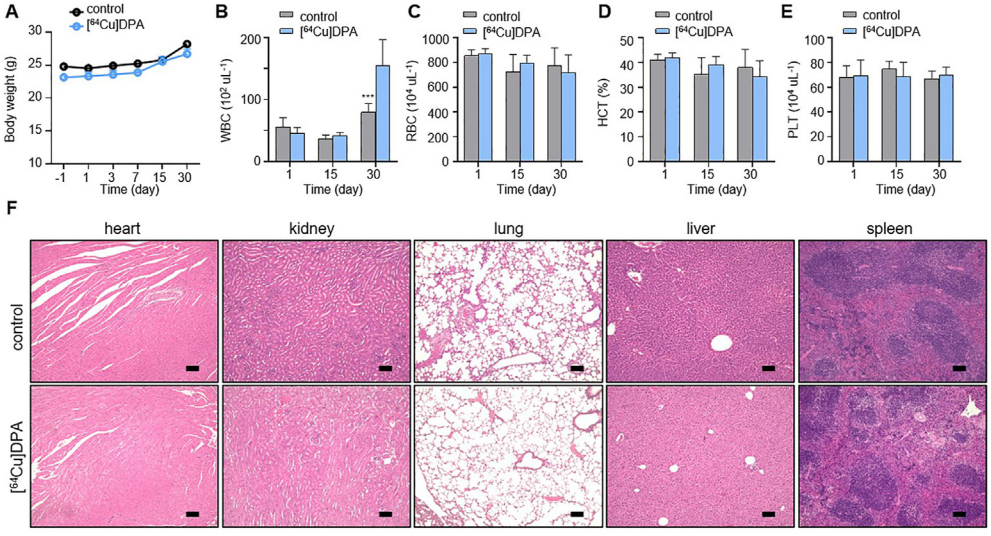

Figure 7 *In vivo* toxicity of [^{64}Cu]DPA. C57BL/6J normal mice received intravenous injection of either saline (control, 200 μL) or [^{64}Cu]DPA (~3 mCi per mice, 200 μL) on day 0. The body weight of mice was measured on days −1, 1, 3, 7, 15, and 30. Fresh blood was drawn from the tail vein under anesthesia on days 1, 15, and 30. The heart, kidney, lung, liver, and spleen were harvested on day 30. (A) Body weight changes in mice. Data are mean ± SD. ($n = 4$ mice/group). (B)–(E) Changes in WBC, RBC, and HCT of C57BL/6J normal mice treated with either saline or [^{64}Cu]DPA. Data are mean ± SD, $n = 4$. (F) Representative H&E staining of the heart, kidney, lung, liver, and spleen from treated C57BL/6J normal mice. Scale bars, 200 μm.

cleared by the renal filtration system. Taken together, these results suggested that [^{64}Cu]DPA is well tolerated at a high dose.

The D-peptide strategy represents a robust and reliable method to remedy the poor *in vivo* stability of native peptides. However, there remain many basic, unresolved questions associated with D-peptides and their use. One of the most important is the *in vivo* fate of D-peptides. Since D-peptides are thought to be non-degradable in the living body, their distribution and elimination are key factors determining their bioavailability and toxicity. To fully realize the potential of D-peptides and facilitate their clinical translation, a comprehensive investigation of the *in vivo* fate of D-peptides is urgently needed. In this study, we harnessed the non-invasive and quantitative nature of PET imaging in conjunction with radiolabeled DPA to study its metabolic profile and target engagement. Our results indicated that DPA was primarily excreted by the kidney-bladder pathway without concomitant degradation. Moreover, the detailed pharmacokinetic and distribution of DPA were profiled in multiple animal models. To the best of our knowledge, this is the first time PET imaging has been used to study the *in vivo* behavior of D-peptides. The results presented in this study also represent the first, quantitative, *in vivo* measurement of D-peptides.

The results gained from this study will help develop long-acting peptide drugs. Regarding this, how to effectively tune kidney excretion to allow for long-acting peptide drugs has remained a challenge. Peptide therapeutics having poor *in vivo* stability and usually exhibit rapid, renal clearance and subsequent low bioavailability. As a result, they require frequent injections and high doses, which severely limits their use and increases cost burden. Given this, long-acting engineering affords a good method for improving overall efficacy. A common strategy used is PEGylation (usually using PEG with MW $>$ 2000 Da) of peptides, which reduces kidney clearance by increasing the size of the drug molecules[59]. However, this approach has been invalidated in some cases, as PEGylation can adversely disrupt the activity of the peptides and/or trigger rare allergic reactions.

Compared to PEGylation, the D-peptide strategy elevates bioavailability by preventing degradation; moreover, it is straightforward and easily accessible. More importantly, it does not change the exact molecular formulation of the peptides. However, the pharmacokinetics and pharmacodynamics of D-peptides remain unknown; in particular, the kidney metabolism of D-peptides. Here, we analyzed the urine of mice injected with [^{64}Cu]DPA and demonstrated that intact DPA was excreted without degradation. Furthermore, our PET imaging results indicated that DPA was rapidly eliminated by the kidney after administration. This implied that DPA had somewhat low bioavailability although it had high stability. A possible approach to slow renal clearance of DPA is multimerization of DPA, which tethers monomers into a polymer. This approach increases the size of the molecules as well as increases their binding affinities. Whether this approach is feasible remains under investigation.

Our study also indicated that D-peptides would be exceptional vectors for radiopharmaceuticals. For instance, we demonstrated that [^{68}Ga]DPA was a better PET tracer than [^{64}Cu]DPA to gauge PL-L1 expression in tumors. This was determined since the decay half-life of ^{68}Ga was more aligned with the target engaging time of DPA. A possible reason for this modest tumor retention may be due to the relatively low binding affinity of DPA for PD-L1. In general, the pharmacodynamics (*i.e.*, target retention and absolute uptake) of D-peptides were expected to be notably improved compared to their L-homologous, especially if their binding affinities were comparable. Since we did not use the L-homologous of DPA as a control in this study, future experiments are warranted to compare in parallel the target engagement between L- and D-peptides. Despite moderate tumor retention, [^{64}Cu]DPA was demonstrated to effectively delay U87MG tumor growth and improve the overall survival of mice. In the future, designing D-peptide ligands with a super binding capacity ($K_D < 10$ nmol/L) will allow for the target engagement of D-peptides to be comparable with that of antibodies. This approach should also show better pharmacokinetics for the D-peptide relative to the bulky antibodies. If this were achieved, we hypothesize that the therapeutic capacity would improve by several orders of magnitude.

4. Conclusions

In conclusion, we non-invasively and quantitatively tracked a D-peptide in living animals and carefully studied its metabolic profile, ability to bind to PD-L1, and therapeutic potential as a TRT agent. The results presented in this study deepen our understanding of the genuine, *in vivo* properties of D-peptides. It is worth noting that the *in vivo*, peptide fate is determined by many factors and is sequence-dependent. Given this, the study of DPA presented here provides a paradigmatic model that is generally applicable to other D-peptides as a way to explore their *in vivo* behaviors. Finally, our insights into DPA's *in vivo* performance offer a valuable reference point for the design of ideal D-peptide drugs; moreover, it paves the way to exploit D-peptides as effective radiopharmaceuticals to manage cancer-both as PET tracers and radiotheranostic agents.

Acknowledgments

We thank the staff of the National Institutes for Quantum and Radiological Sciences and Technology (QST) for their support in cyclotron operation, radioisotope production, radiosynthesis, and animal experiments. We sincerely thank the financial support from the JSPS KAKENHI grant Nos. 19K17156, 21H02873, 21K07659, and 20H03635, Japan. This research is also supported by QST President's Strategic Grant (Exploratory Research, Japan). We also thank the financial support from the National Natural Science Foundation of China (82003532), General Project of Science and Technology Development Fund of Nanjing Medical University (NMUB2019154, China), the second round of Nanjing Clinical Medical Center "Nanjing Nuclear Medicine Center", and the China Postdoctoral Science Foundation (2019M650302).

Author contributions

Kuan Hu and Mingrong Zhang designed research; Kuan Hu, Wenyu Wu, Lin Xie, Yiding Zhang, Masayuki Hanyu, LuLu Zhang, Yinghuan Liu, Kotaro Nagatsu, and Hisashi Suzuki performed research; Hao Geng and Yundong Wu performed computational simulations; Kuan Hu, Wenyu Wu, and Hao Geng analyzed data; Kuan Hu, Wenyu Wu, Zigang Li, Feng Wang, and Mingrong Zhang discussed the results; Yundong Wu, Zigang Li, Feng Wang, and Mingrong Zhang supervised the research; Jialin Guo edited the manuscript; Kuan Hu, Wenyu Wu, Hao Geng, Yundong Wu and Mingrong Zhang wrote the manuscript.

Conflicts of interest

The authors have no conflicts of interest to declare.

Appendix A. Supporting information

Supporting information to this article can be found online at https://doi.org/10.1016/j.apsb.2021.09.016.

References

1. Fosgerau K, Hoffmann T. Peptide therapeutics: current status and future directions. *Drug Discov Today* 2015;**20**:122–8.
2. Lau JL, Dunn MK. Therapeutic peptides: historical perspectives, current development trends, and future directions. *Bioorg Med Chem* 2018;**26**:2700–7.
3. Drucker DJ. Advances in oral peptide therapeutics. *Nat Rev Drug Discov* 2020;**19**:277–89.
4. Otvos L, Wade JD. Current challenges in peptide-based drug discovery. *Front Chem* 2014;**2**:62.
5. Tugyi R, Uray K, Iván D, Fellinger E, Perkins A, Hudecz F. Partial D-amino acid substitution: improved enzymatic stability and preserved Ab recognition of a MUC2 epitope peptide. *Proc Natl Acad Sci U S A* 2005;**102**:413–8.
6. Chorev M. The partial retro-inverso modification: a road traveled together. *Biopolymers* 2005;**80**:67–84.
7. Fletcher MD, Campbell MM. Partially modified retro-inverso peptides: development, synthesis, and conformational behavior. *Chem Rev* 1998;**98**:763–96.
8. Uppalapati M, Lee DJ, Mandal K, Li H, Miranda LP, Lowitz J, et al. A potent D-protein antagonist of VEGF-A is nonimmunogenic, metabolically stable, and longer-circulating *in vivo*. *ACS Chem Biol* 2016;**11**:1058–65.
9. Garton M, Nim S, Stone TA, Wang KE, Deber CM, Kim PM. Method to generate highly stable D-amino acid analogs of bioactive helical peptides using a mirror image of the entire PDB. *Proc Natl Acad Sci U S A* 2018;**115**:1505–10.
10. Rabideau AE, Pentelute BL. A D-Amino acid at the N-terminus of a protein abrogates its degradation by the N-end rule pathway. *ACS Cent Sci* 2015;**1**:423–30.
11. Jia F, Wang J, Peng J, Zhao P, Kong Z, Wang K, et al. D-amino acid substitution enhances the stability of antimicrobial peptide polybia-CP. *Acta Biochim Biophys Sin* 2017;**49**:916–25.
12. Carmona G, Rodriguez A, Juarez D, Corzo G, Villegas E. Improved protease stability of the antimicrobial peptide Pin2 substituted with D-amino acids. *Protein J* 2013;**32**:456–66.
13. Feng Z, Xu B. Inspiration from the mirror: D-amino acid containing peptides in biomedical approaches. *Biomol Concepts* 2016;**7**:179–87.
14. Lau YH, de Andrade P, Wu Y, Spring DR. Peptide stapling techniques based on different macrocyclisation chemistries. *Chem Soc Rev* 2015;**44**:91–102.
15. White CJ, Yudin AK. Contemporary strategies for peptide macrocyclization. *Nat Chem* 2011;**3**:509–24.
16. Appella DH, Christianson LA, Karle IL, Powell DR, Gellman SH. β-Peptide foldamers: robust helix formation in a new family of β-amino acid oligomers. *J Am Chem Soc* 1996;**118**:13071–2.
17. Qvit N, Rubin SJS, Urban TJ, Mochly-Rosen D, Gross ER. Peptidomimetic therapeutics: scientific approaches and opportunities. *Drug Discov Today* 2017;**22**:454–62.
18. Schumacher TNM, Mayr LM, Minor DL, Milhollen MA, Burgess MW, Kim PS. Identification of D-peptide ligands through mirror-image phage display. *Science* 1996;**271**:1854–7.
19. Chorev M, Goodman M. A dozen years of retro-inverso peptidomimetics. *Acc Chem Res* 1993;**26**:266–73.
20. Zhou N, Luo Z, Luo J, Fan X, Cayabyab M, Hiraoka M, et al. Exploring the stereochemistry of CXCR4-peptide recognition and inhibiting HIV-1 entry with D-peptides derived from chemokines. *J Biol Chem* 2002;**277**:17476–85.
21. Sakurai K, Chung HS, Kahne D. Use of a retroinverso p53 peptide as an inhibitor of MDM2. *J Am Chem Soc* 2004;**126**:16288–9.
22. Welch BD, VanDemark AP, Heroux A, Hill CP, Kay MS. Potent D-peptide inhibitors of HIV-1 entry. *Proc Natl Acad Sci U S A* 2007;**104**:16828–33.
23. Liu M, Li C, Pazgier M, Li C, Mao Y, Lv Y, et al. D-peptide inhibitors of the p53–MDM2 interaction for targeted molecular therapy of malignant neoplasms. *Proc Natl Acad Sci U S A* 2010;**107**:14321–6.
24. Zhan C, Zhao L, Wei X, Wu X, Chen X, Yuan W, et al. An ultrahigh affinity D-peptide antagonist of MDM2. *J Med Chem* 2012;**55**:6237–41.
25. Wei X, Zhan C, Chen X, Hou J, Xie C, Lu W. Retro-inverso isomer of Angiopep-2: a stable d-peptide ligand inspires brain-targeted drug delivery. *Mol Pharm* 2014;**11**:3261–8.
26. Zhou X, Zuo C, Li W, Shi W, Zhou X, Wang H, et al. A Novel D-peptide identified by mirror-image phage display blocks TIGIT/PVR for cancer immunotherapy. *Angew Chem Int Ed Engl* 2020;**59**:15114.
27. Chang HN, Liu BY, Qi YK, Zhou Y, Chen YP, Pan KM, et al. Blocking of the PD-1/PD-L1 interaction by a D-peptide antagonist for cancer immunotherapy. *Angew Chem Int Ed Engl* 2015;**54**:11760–4.
28. Li H, Kem DC, Zhang L, Huang B, Liles C, Benbrook A, et al. Novel retro-inverso peptide inhibitor reverses angiotensin receptor autoantibody-induced hypertension in the rabbit. *Hypertension* 2015;**65**:793–9.
29. Luo Z, Wu Q, Yang C, Wang H, He T, Wang Y, et al. A Powerful CD8+T-cell stimulating D-tetra-peptide hydrogel as a very promising vaccine adjuvant. *Adv Mater* 2017;**29**:1601776.
30. Vaissiere A, Aldrian G, Konate K, Lindberg MF, Jourdan C, Telmar A, et al. A retro-inverso cell-penetrating peptide for siRNA delivery. *J Nanobiotechnol* 2017;**15**:34.
31. Guichard G, Benkirane N, Zeder-Lutz G, van Regenmortel MH, Briand JP, Muller S. Antigenic mimicry of natural L-peptides with retro-inverso-peptidomimetics. *Proc Natl Acad Sci U S A* 1994;**91**:9765–9.
32. Wermuth J, Goodman SL, Jonczyk A, Kessler H. Stereoisomerism and biological activity of the selective and superactive $\alpha v\beta 3$ integrin inhibitor cyclo(-RGDfV-) and its retro-inverso peptide. *J Am Chem Soc* 1997;**119**:1328–35.
33. Kannan S, Aronica PGA, Ng S, Gek Lian DT, Frosi Y, Chee S, et al. Macrocyclization of an all-D linear alpha-helical peptide imparts cellular permeability. *Chem Sci* 2020;**11**:5577–91.
34. Du S, Luo C, Yang G, Gao H, Wang Y, Li X, et al. Developing PEGylated reversed D-peptide as a novel HER2-targeted SPECT imaging probe for breast cancer detection. *Bioconjugate Chem* 2020;**31**:1971–80.
35. Subramanian R, Zhu X, Kerr SJ, Esmay JD, Louie SW, Edson KZ, et al. Nonclinical pharmacokinetics, disposition, and drug–drug interaction potential of a novel D-amino acid peptide agonist of the calcium-sensing receptor AMG 416 (etelcalcetide). *Drug Metab Dispos* 2016;**44**:1319–31.
36. Veine DM, Yao H, Stafford DR, Fay KS, Livant DL. A D-amino acid containing peptide as a potent, noncovalent inhibitor of $\alpha 5\beta 1$ integrin in human prostate cancer invasion and lung colonization. *Clin Exp Metastasis* 2014;**31**:379–93.
37. Jung KO, Kim TJ, Yu JH, Rhee S, Zhao W, Ha B, et al. Whole-body tracking of single cells *via* positron emission tomography. *Nat Biomed Eng* 2020;**4**:835–44.
38. Fani M, Maecke H, Okarvi S. Radiolabeled peptides: valuable tools for the detection and treatment of cancer. *Theranostics* 2012;**2**:481.
39. Liu Z, Pourghiasian M, Radtke MA, Lau J, Pan J, Dias GM, et al. An organotrifluoroborate for broadly applicable one-step ^{18}F-labeling. *Angew Chem Int Ed Engl* 2014;**53**:11876–80.
40. Jackson IM, Scott PJH, Thompson S. Clinical applications of radiolabeled peptides for PET. *Semin Nucl Med* 2017;**47**:493–523.
41. Hu K, Shang J, Xie L, Hanyu M, Zhang Y, Yang Z, et al. PET imaging of VEGFR with a novel ^{64}Cu-labeled peptide. *ACS Omega* 2020;**5**:8508–14.
42. Hu K, Xie L, Hanyu M, Zhang Y, Li L, Ma X, et al. Harnessing the PD-L1 interface peptide for positron emission tomography imaging of the PD-1 immune checkpoint. *RSC Chem Biol* 2020;**1**:214–24.

43. Hu K, Hanyu M, Xie L, Zhang Y, Nagatsu K, Suzuki H, et al. Correction: developing native peptide-based radiotracers for PD-L1 PET imaging and improving imaging contrast by pegylation. *Chem Commun* 2019;**55**:4273.
44. Adessi C, Soto C. Converting a peptide into a drug: strategies to improve stability and bioavailability. *Curr Med Chem* 2002;**9**:963−78.
45. Bullock BN, Jochim AL, Arora PS. Assessing helical protein interfaces for inhibitor design. *J Am Chem Soc* 2011;**133**:14220−3.
46. Patel SP, Kurzrock R. PD-L1 expression as a predictive biomarker in cancer immunotherapy. *Mol Canc Therapeut* 2015;**14**:847−56.
47. Stangl S, Tei L, De Rose F, Reder S, Martinelli J, Sievert W, et al. Preclinical evaluation of the Hsp70 peptide tracer TPP-PEG24-DFO[(89)Zr] for tumor-specific PET/CT imaging. *Cancer Res* 2018;**78**:6268−81.
48. Miller MM, Wasik SP, Huang GL, Shiu WY, Mackay D. Relationships between octanol-water partition coefficient and aqueous solubility. *Environ Sci Technol* 1985;**19**:522−9.
49. Tencer J, Frick IM, Oquist BW, Alm P, Rippe B. Size-selectivity of the glomerular barrier to high molecular weight proteins: upper size limitations of shunt pathways. *Kidney Int* 1998;**53**:709−15.
50. Wartiovaara J, Ofverstedt LG, Khoshnoodi J, Zhang J, Mäkelä E, Sandin S, et al. Nephrin strands contribute to a porous slit diaphragm scaffold as revealed by electron tomography. *J Clin Invest* 2004;**114**:1475−83.
51. Wu HN, Jiang F, Wu YD. Significantly improved protein folding thermodynamics using a dispersion-corrected water model and a new residue-specific force field. *J Phys Chem Lett* 2017;**8**:3199−205.
52. Jiang F, Wu HN, Kang W, Wu YD. Developments and applications of Coil-library-based residue-specific force fields for molecular dynamics simulations of peptides and proteins. *J Chem Theor Comput* 2019;**15**:2761−73.
53. Qiu XY, Hu DX, Chen WQ, Chen RQ, Qian SR, Li CY, et al. PD-L1 confers glioblastoma multiforme malignancy *via* Ras binding and Ras/Erk/EMT activation. *Biochim Biophys Acta (BBA) - Mol Basis Dis* 2018;**1864**:1754−69.
54. Maecke HR, Hofmann M, Haberkorn U. ^{68}Ga-labeled peptides in tumor imaging. *J Nucl Med* 2005;**46**:172S−8S.
55. Herrmann K, Schwaiger M, Lewis JS, Solomon SB, McNeil BJ, Baumann M, et al. Radiotheranostics: a roadmap for future development. *Lancet Oncol* 2020;**21**:e146−56.
56. Sgouros G, Bodei L, McDevitt MR, Nedrow JR. Radiopharmaceutical therapy in cancer: clinical advances and challenges. *Nat Rev Drug Discov* 2020;**19**:589−608.
57. Jin ZH, Tsuji AB, Degardin M, Sugyo A, Obara S, Wakizaka H, et al. Radiotheranostic agent ^{64}Cu-cyclam-RAFT-c(-RGDfK-)$_4$ for management of peritoneal metastasis in ovarian cancer. *Clin Canc Res* 2020;**26**:6230−41.
58. Tang C, Gomez DR, Wang H, Levy LB, Zhuang Y, Xu T, et al. Association between white blood cell count following radiation therapy with radiation pneumonitis in non-small cell lung cancer. *Int J Radiat Oncol Biol Phys* 2014;**88**:319−25.
59. Harris JM, Chess RB. Effect of pegylation on pharmaceuticals. *Nat Rev Drug Discov* 2003;**2**:214−21.